



RESEARCH ARTICLE

10.1002/2016JD026252

Key Points:

- Characterization of an exceptional winter Saharan dust event leading to surpass the PM₁₀ EU daily limit
- Spatial, temporal, and vertical distribution synergistically investigated
- Modelled dust vertical distribution agreed well with measurements

Supporting Information:

- Supporting Information S1

Correspondence to:

G. Titos,
gloria.titos@idaea.csic.es

Citation:

Titos, G., M. Ealo, M. Pandolfi, N. Pérez, Y. Sola, M. Sicard, A. Comerón, X. Querol, and A. Alastuey (2017), Spatiotemporal evolution of a severe winter dust event in the western Mediterranean: Aerosol optical and physical properties, *J. Geophys. Res. Atmos.*, 122, 4052–4069, doi:10.1002/2016JD026252.

Received 17 NOV 2016

Accepted 28 MAR 2017

Accepted article online 29 MAR 2017

Published online 14 APR 2017

Spatiotemporal evolution of a severe winter dust event in the western Mediterranean: Aerosol optical and physical properties

G. Titos¹ , M. Ealo^{1,2}, M. Pandolfi¹, N. Pérez¹ , Y. Sola² , M. Sicard^{3,4} , A. Comerón³ , X. Querol¹ , and A. Alastuey¹

¹Department of Geosciences, Institute of Environmental Assessment and Water Research, CSIC, Barcelona, Spain, ²Group of Meteorology, Department of Applied Physics, Faculty of Physics, University of Barcelona, Barcelona, Spain, ³Remote Sensing Laboratory, Universitat Politècnica de Catalunya, Barcelona, Spain, ⁴Ciències i Tecnologies de l'Espai - Centre de Recerca de l'Aeronàutica i de l'Espai/ Institut d'Estudis Espacials de Catalunya, Universitat Politècnica de Catalunya, Barcelona, Spain

Abstract An outstanding Saharan dust event affected the Iberian Peninsula during winter 2016 (20 to 25 February). The impact of this event on ambient PM₁₀ surface levels and its spatial and temporal evolution was investigated by means of data from 250 air quality stations across mainland Spain and the Balearic Islands. The event had a significant impact on surface PM₁₀ levels, and on 22 February, 90% of the air quality monitoring sites registered PM₁₀ concentrations above the EU daily limit value of 50 μg/m³. The study of the attenuated backscattering vertical profiles associated with African dust evidenced a complex structure, with a thick aerosol layer that was at higher altitudes over the pre-Pyrenees compared to the coastal area of Barcelona but closer to the surface than typically observed at both sites. Optical and physical properties of dust particles were investigated at the continental background Global Atmosphere Watch mountain observatory of Montsec (MSA) in the pre-Pyrenees. Good agreement was found between in situ and passive remote sensing methodologies once the aloft dust layer reached the MSA station. Scattering Ångström exponent values decreased to values close to zero (even below zero for surface in situ measurements) indicating the predominance of coarse particles. On the contrary, absorption Ångström exponent values increased during the Saharan dust outbreak denoting an absorption enhancement at shorter wavelengths, characteristic of mineral dust particles. Furthermore, the performance of NMMB/BSC-Dust and BSC-DREAM8b models has been qualitatively evaluated for the dust spatial distribution across Spain and the vertical structure over MSA and Barcelona showing good agreement.

1. Introduction

Mineral dust is, after sea spray, the major constituent of airborne particles on the global scale [Intergovernmental Panel on Climate Change (IPCC), 2013]. Mineral dust particles are emitted mainly by disintegration of aggregates following creeping and saltation of larger soil particles over desert and other arid surfaces [e.g., IPCC, 2013, and references therein]. The magnitude of dust emissions into the atmosphere depends on the surface wind speed and a number of soil-related factors, such as texture, moisture, and vegetation cover. Because of the large amount of factors involved, the range of estimates of possible dust emissions spans widely. For example, the estimate for North Africa is 400 to 2200 Tg/yr [Huneeus et al., 2011].

Mineral dust plays an important role in the Earth's climate through interacting with both solar and thermal infrared radiation [e.g., Tegen et al., 1996; Antón et al., 2014]. It has also significant implications for cloud microphysics [e.g., Creamean et al., 2013], atmospheric chemistry [e.g., Querol et al., 2009], human health [e.g., Perez et al., 2008; Pandolfi et al., 2014a], and the carbon cycle via the fertilization of marine and terrestrial ecosystems [e.g., Koren et al., 2006]. A great attention has been paid over the last years to characterize dust transport processes in the western Mediterranean [Rodríguez et al., 2001; Escudero et al., 2005; Querol et al., 2009; Pey et al., 2013; Salvador et al., 2014] and their impact on dust surface concentrations [e.g., Querol et al., 1998, 2009; Rodríguez et al., 2011; Cabello et al., 2012; Pey et al., 2013; Salvador et al., 2013; Cachorro et al., 2016] and aerosol optical properties [e.g., Valenzuela et al., 2012a, 2012b, 2015]. Despite this, up to date, atmospheric mineral dust is still recognized as one of the main uncertainties in climate change projections [IPCC, 2013], related to its high temporal and spatial variability, different transport pathways, and vertical distribution in the atmosphere, among other factors.

©2017. The Authors.

This is an open access article under the terms of the Creative Commons Attribution-NonCommercial-NoDerivs License, which permits use and distribution in any medium, provided the original work is properly cited, the use is non-commercial and no modifications or adaptations are made.

In the Northern Hemisphere, the Sahara desert is the most important source of mineral dust [e.g., Prospero *et al.*, 2002]. Due to its proximity to the African continent, the Iberian Peninsula is frequently affected by Saharan dust outbreaks. A clear summer prevalence of dust events is observed in the western Mediterranean with low occurrence of severe episodes [Pey *et al.*, 2013]. In regional background sites of the western Mediterranean, African dust is an important aerosol source accounting from 10 up to 25% of PM₁₀ on an annual average (up to 45% in high mountain areas in the southwestern Mediterranean) [Pey *et al.*, 2013]. Thus, African dust is an important source of particulate matter pollution in southern Europe, decisively contributing to surpass the 35 annual exceedances of the daily limit (DL) value of 50 $\mu\text{g}/\text{m}^3$ fixed by the European Air Quality Directive 2008/50/EC. This Directive also allows excluding of the annual counting the exceedances attributable to natural sources, such as African dust, if appropriate scientific support of their causes is provided. One of the methods officially accepted by the European Commission [European Commission (EC), 2011] to demonstrate the natural cause of such exceedances considers that the daily net dust load in PM₁₀ attributable to an African event in a given region can be obtained by subtracting the daily regional background level (PM₁₀ measured just before and after the episode) from the PM₁₀ concentration (daily measured during the African dust episode) [Escudero *et al.*, 2007; EC, 2011].

Long-term studies in African dust outbreaks have been proven to be useful for investigating average dust properties in terms of seasonal patterns and recurrent transport scenarios [e.g., Papayannis *et al.*, 2005; Valenzuela *et al.*, 2012a; Toledano *et al.*, 2007; Burgos *et al.*, 2016; Sicard *et al.*, 2016a]. However, the complexity of these events in terms of intensity, duration, and vertical distribution makes each event unique. This has led to significant research on specific events of moderate and severe intensity. Most of these studies focused on column-integrated aerosol properties alone [e.g., Lyamani *et al.*, 2005; Basart *et al.*, 2009; Pavese *et al.*, 2012; Obregon *et al.*, 2015] or combined column integrated with vertically resolved aerosol optical properties [e.g., Papayannis *et al.*, 2007; Guerrero-Rascado *et al.*, 2009; Córdoba-Jabonero *et al.*, 2011; Bravo-Aranda *et al.*, 2015; Gkikas *et al.*, 2016]. In this study, we perform a comprehensive analysis of a severe dust event affecting the Iberian Peninsula during February 2016. Hourly PM₁₀ concentrations measured at 250 air quality (AQ) monitoring stations across mainland Spain and the Balearic Islands were used to study the spatial and temporal distribution of the dust plume and its impact at surface level. Additionally, a synergetic analysis of aerosol in situ and remote sensing (passive and active) measurements performed at Montsec observatory (pre-Pyrenees, northeastern Spain) allowed us to characterize dust optical properties and its vertical distribution during the dust event. The comparison between the different techniques (in situ and remote sensing) has been evaluated as well. Finally, the vertical and horizontal patterns obtained with experimental data were compared with the outputs of the of NMMB/BSC-Dust and BSC-DREAM8b models.

2. Experimental

2.1. Monitoring Sites

The study area covers mainland Spain and the Balearic Islands. PM₁₀ concentrations were obtained from 250 AQ stations managed by AQ monitoring networks of the different regional governments in Spain. All AQ stations used in this study provide hourly PM₁₀ concentrations measured by either Tapered Oscillating Microbalance [Patashnick and Rupprecht, 1991] or Beta-gauge Attenuation techniques [Chow, 1995] and comply with the quality control requirements from the 2008/50/CE Directive and report data to the EC for AQ evaluation.

Results on aerosol optical and physical properties were obtained from measurements performed in the northeastern Iberian Peninsula, at the Montsec station (MSA; 42°3'N, 0°44'E, 1570 m above sea level (asl)). The MSA continental background site is integrated in the Global Atmosphere Watch (GAW) program and in the European Research Infrastructure ACTRIS (Aerosols, Clouds, and Trace gases Research Infrastructure; www.actris.eu). It is a remote high-altitude station situated in the southern side of the pre-Pyrenees at the Montsec d'Ares mountain, 140 km northwest of Barcelona. Detailed information on MSA monitoring station can be found in Ripoll *et al.* [2014] and Pandolfi *et al.* [2014b]. Ancillary data gathered at Barcelona urban area were used to support the interpretation of the results. The instrumentation was located in the North Campus of the Universitat Politècnica de Catalunya (BCN; 2°7'E, 41°23'N, 115 m asl), approximately 1 km from Sierra de Collserola and 7 km from the sea.

2.2. Surface In Situ Measurements

Aerosol particle light scattering (σ_{sp}) and hemispheric backscattering (σ_{bsp}) coefficients were measured at three wavelengths, λ (450, 525, and 635 nm) with a LED-based integrating nephelometer (model Aurora 3000, ECOTECH Pty, Ltd, Knoxfield, Australia) with 5 min time resolution. The aerosol flow in the nephelometer was set to 5 Lpm. The nephelometer is periodically calibrated (3 times per year) with CO₂ and filtered air. Zero adjusts are performed daily by using internally filtered particle free air. The experimental design of the nephelometer limits the collection of radiation scattered around both the backward (180°) and forward (0°) directions. The Aurora 3000 nephelometer used in this study operates by collecting light scattered within the angular range 10–171° [Müller *et al.*, 2011a]. The main source of error is the truncation in the forward direction (0–10°) due to the inability of the nephelometer to sense near-forward scattering, which is an increasingly dominant part of the total scattering for large particles [Anderson *et al.*, 1996]. Nonidealities due to truncation errors have been corrected following the procedure described in Müller *et al.* [2011a]. The detection limits of the nephelometer over 1 min averaging time are 0.11, 0.14, and 0.12 Mm⁻¹ for total scattering at 450, 525 and 635 nm, respectively, and 0.12, 0.11 and 0.13 Mm⁻¹ for backscattering [Müller *et al.*, 2011a].

The aerosol light absorption coefficient, σ_{apr} , was measured with a multiangle absorption photometer (MAAP, model 5012, Thermo) at 637 nm [Müller *et al.*, 2011b]. A detailed description of the method is provided by Petzold and Schönlinner [2004]. The MAAP draws the ambient air at constant flow rate of 16.7 Lpm and provides 1 min values. The detection limit of the MAAP instrument is lower than 0.6 Mm⁻¹ over 2 min integration. The total method uncertainty for the particle light absorption coefficient inferred from MAAP measurement is around 12% [Petzold and Schönlinner, 2004]. Multiwavelength aerosol light absorption measurements were performed with an aethalometer [Hansen *et al.*, 1984] model AE33, (Aerosol d.o.o.) at seven nominal wavelengths (370, 470, 520, 590, 660, 880, and 950 nm) and at 1 min time resolution. Aerosol flow in this instrument was set to 5 Lpm. Drinovec *et al.* [2015] presented the working principle and main characteristics of this instrument. Uncertainty of this instrument is about ±5% [Hansen, 2005; Drinovec *et al.*, 2015].

An aerosol optical counter (GRIMM Spectrometer, model 1129-Sky-OPC) was used to determine particle number concentrations in 31 size bins, for particles in the size range from 0.25 to 32 μm at 5 min time resolution. The working principle of this instrument is based on multichannel light-scattering optics [Grimm and Eatough, 2009]. The intensity of the measured scattered light is related with the size of the particles. The instrument is factory standardized versus a mother unit that is calibrated with polystyrene latex (PSL) for tuning the algorithm that relates the measured scattered light with particle size. Since the refractive index of PSL (1.59) is different from that of the ambient aerosol, it is possible that the factory calibration does not reproduce correctly the scattering properties of the sampled aerosol and therefore it can provide an erroneous estimation of the particles diameter. The particle diameters (D_p) were recalculated from original refractive index to the refractive index of dust (1.53–0.001i) [Pío *et al.*, 2014] that is the predominant aerosol type during this episode. Mass and volume size distributions were derived from the measured number size distribution assuming spherical particles. A density of 2.5 g/cm³, characteristic of dust [Pío *et al.*, 2014], was used to calculate the mass size distribution from the number size distribution.

All in situ measurements refer to ambient conditions and were performed at low relative humidity (RH < 40%), as recommended by the World Meteorological Organization [World Meteorological Organization, 2003] and ACTRIS infrastructure.

2.3. Passive Remote Sensing Measurements

Measurements of column-integrated aerosol properties were obtained at MSA station using a Sun photometer (CIMEL CE-318) included in AERONET (Aerosol Robotic Network) [Holben *et al.*, 1998]. This instrument performs direct Sun measurements with a 1.2° full field of view at 340, 380, 440, 500, 675, 870, and 1020 nm. The sky radiance measurements (almucantar configuration) are carried out at 440, 670, 870, and 1020 nm. A full description of this instrument can be found in Holben *et al.* [1998]. The uncertainty in the retrieval of aerosol optical depth (AOD) under cloud free conditions is ±0.01 for wavelengths larger than 440 nm and ±0.02 for shorter wavelengths [Eck *et al.*, 1999]. Errors in aerosol size distribution retrievals depend on particle size, aerosol type, and actual values of the size distribution. For particles in the size range 0.1 < r < 7 μm, retrieval

errors are around 10–35%, while for sizes lower than 1 μm and higher than 7 μm retrieval errors rise up to 80–100% [Dubovik *et al.*, 2000]. For measurements under low aerosol load conditions (i.e., AOD (440 nm) < 0.2), the retrievals accuracy decrease significantly [Dubovik and King, 2000; Dubovik *et al.*, 2000]. In this work, the AERONET level 1.5 data are used, including the aerosol optical depth (AOD) and inversion products derived from the almucantar radiances. No level 2 retrievals were available at MSA during this dust event due to strong limitations imposed by AERONET inversion algorithm (AOD (440 nm) > 0.4 and solar zenith angle > 50°). In this sense, other studies have successfully employed level 1.5 AERONET data [e.g., Lyamani *et al.*, 2012; Obregon *et al.*, 2015]. The absorption optical depth, AAOD, was calculated from the aerosol optical depth, AOD, and the single scattering albedo, SSA [Russell *et al.*, 2010]. The scattering-related optical depth was obtained by subtracting the AAOD from the AOD.

2.4. Active Remote Sensing Measurements

Vertical profiles of attenuated backscatter, β_{att} , were performed with a Jenoptik CHM 15 k ceilometer that includes a pulsed Nd:YAG laser, emitting at 1064 nm. The energy emitted per pulse is 8 μJ , and the duration of each pulse is between 1 and 5 ns with a repetition frequency of 6.5 kHz. This instrument operates continuously with a temporal resolution of 60 s and a spatial resolution of 15 m. The maximum height of the signal is 15.36 km above ground level (agl) equivalent to 1024 range bins. In this work, calibration based on the Rayleigh calibration method [Bucholtz, 1995; Wiegner *et al.*, 2014] is used. This method compares the range-corrected signal retrieved by the ceilometer in a region free of particles with respect to the attenuated molecular backscatter in the same region (known by Rayleigh theory). The overlap of the telescope and the laser beam is greater than 90% at around 600 m agl. The ceilometer is strategically located 760 m downslope of MSA measurement station. Therefore, at the altitude of MSA the full overlap is likely achieved. The short horizontal distance between the ceilometer and the MSA station (less than 2.5 km) guarantees that the sampled air masses by the ceilometer and by the instrumentation deployed at MSA station are the same.

At BCN site, profiles of the attenuated backscatter were measured with a micropulse lidar (MPL) system, model MPL-4B, at 532 nm. The MPL system is a compact, eye-safe lidar designed for full time unattended operation [Spinhirne, 1993; Campbell *et al.*, 2002; Flynn *et al.*, 2007]. It uses a pulsed solid-state laser emitting low-laser pulse energy (6 μJ) at a pulse rate of 2.5 kHz and a coaxial transceiver design with a telescope shared by both transmission and reception optics. In nominal operation the raw temporal and vertical resolutions are 30 s and 15 m, respectively. A method similar to the one used for the ceilometer was employed to retrieve the attenuated backscatter coefficient from the MPL data. The molecular optical properties were calculated with Rayleigh theory and local radiosoundings measurements. A detail description of the system layout can be found in Sicard *et al.* [2016b].

Lidars and ceilometers principle of measurement is the same, and retrieving optical properties in both systems follow the lidar equation:

$$P(z) = C_L^* \frac{O(z)}{z^2} \beta(z) \cdot T^2(z), \quad (1)$$

where $P(z)$ is the flux of backscattered energy received in the telescope from a distance z . The term z^2 accounts for the beam divergence and the increase of the area illuminated with the distance to the laser. The backscattered signal collected by the telescope depends on the overlap between the laser beam and the telescope field of view, and the degree of overlap is quantified by $O(z)$. $\beta(z)$ is the atmospheric backscatter coefficient, and $T(z)$ estimates the atmospheric transmittance of the laser signal (squared due to travel back and forth). C_L^* is a constant that depends on the geometry and characteristics of the instrument and on universal constants.

In equation (1) the only properties depending on the medium are $\beta(z)$ and $T(z)$. Thus, the atmospheric attenuated backscatter is defined as follows:

$$\beta_{\text{att}}(z) = \beta(z) \cdot T^2(z). \quad (2)$$

This variable is not instrument dependent and only depends on the characteristic of the medium, being the β_{att} profiles from the ceilometer and MPL systems directly comparable.

2.5. Derived Intensive Parameters

In addition to the direct measurements obtained with the above detailed instrumentation, the following aerosol intensive parameters have been calculated from the in situ and Sun photometer data.

1. The scattering Ångström exponent (SAE) characterizes the wavelength dependence of the scattering process. For the nephelometer measurements, it is calculated as a linear fit of the scattering coefficients measured in the spectral range 450–635 nm. Similarly, for column-integrated measurements, it is calculated using the scattering-related AOD in the spectral range 440–870 nm. The SAE increases with decreasing particle size and takes values greater than 1.5 when the scattering process is dominated by fine particles, while it is close to 0 when the scattering process is dominated by coarse particles [Seinfeld and Pandis, 1998; Schuster *et al.*, 2006].
2. The absorption Ångström exponent (AAE) has been calculated similarly to the SAE but in the wavelength range 370–950 nm for the absorption coefficient and 440–880 nm for the absorption optical depth. It describes the wavelength dependence of the aerosol absorption properties, and it can give information on the predominant aerosol type or source [e.g., Cazorla *et al.*, 2013; Ealo *et al.*, 2016]. In this sense, black carbon has an AAE equal or close to 1, while brown carbon and mineral dust have an enhanced absorption in the ultraviolet and blue spectral regions yielding an AAE greater than 1 [Kirchstetter *et al.*, 2004; Valenzuela *et al.*, 2015].
3. The single scattering albedo (SSA) is calculated as the ratio of the scattering to the extinction coefficients, providing information on the relative importance of absorption and scattering in the extinction process. It has been calculated at the seven wavelengths of the aethalometer. The SSA spectral dependence, SSAE, provides general information about the aerosol type combining both physical and chemical properties, and it has been shown to be a good indicator of the presence of dust in the atmosphere [Collaud Coen *et al.*, 2004; Costabile *et al.*, 2013]. During Saharan dust outbreaks, a reduction of SAE and a simultaneous increase of AAE lead to negative SSAE values depending on the degree of local pollution and intensity of the Saharan dust event [Ealo *et al.*, 2016].

2.6. Additional Data

The synoptic scenario and the meteorological interpretation were investigated based on synoptic charts of 850 hPa geopotential heights from the NCEP (National Centers for Environmental Prediction) reanalysis. The temporal evolution of the desert dust transport and its impact at surface level and in the atmospheric column were analyzed using information obtained from the output of the NMMB/BSC-Dust and BSC-DREAM8b v2.0 models from the Barcelona Dust Forecast Center (<http://dust.aemet.es>), as well as satellite imagery from Meteosat RGB Dust composites (EUMETSAT, <http://oiswww.eumetsat.org/IPPS/html/MSG/RGB/DUST/>).

3. Results

3.1. The African Dust Outbreak of 20–25 February 2016

As explained in section 1, desert dust outbreaks affect the Iberian Peninsula more frequently during spring and summer months [Querol *et al.*, 1998, 2009; Rodríguez *et al.*, 2001; Escudero *et al.*, 2005; Pey *et al.*, 2013; Cachorro *et al.*, 2016]. Winter events are less frequent but usually of higher intensity [Prospero *et al.*, 2002]. Recently, a severe desert dust outbreak affected the Iberian Peninsula from 20 to 25 February 2016 with high impact on surface PM₁₀ levels. The evolution of the dust outbreak is illustrated in Figure S1 in the supporting information where a sequence of the false color RGB dust images from EUMETSAT imagery (<http://oiswww.eumetsat.org/>) is shown. The dust plume entered the Iberian Peninsula on 21 February from the southeast (Figures S1a–S1c) and then moved to the center and west of the Iberian Peninsula. As the dust plume moved westward, a second plume entered on the afternoon of 21 February through the southeast and moved to the north travelling through the easternmost part of Spain (Figure S1f). On 23 February, due to the change in the synoptic conditions and prevalence of westerly flow, the first plume changed its trajectory and started moving toward the east (Figure S1h).

The synoptic scenario responsible of the dust mobilization and consequent transport is shown in Figure 1 by means of 850 hPa geopotential height from 20 to 25 February 2016. The synoptic situation was characterized by a high-pressure dipole with centers over Azores and Algeria-Tunisia region and a low-pressure system

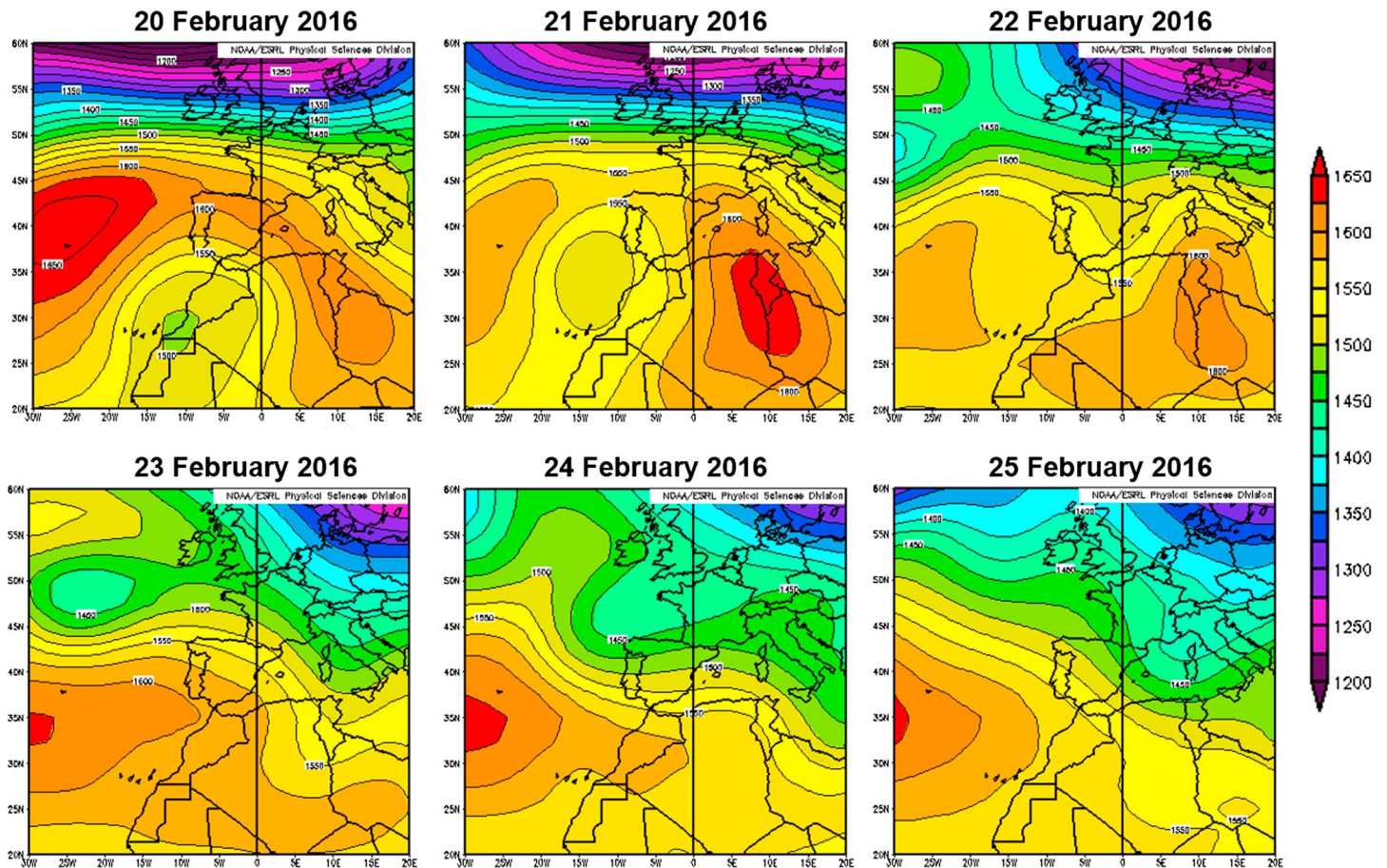


Figure 1. Daily evolution of 850 mb geopotential heights (m) (NCEP/NCAR reanalysis) for the period 20 to 25 February 2016.

over Morocco and Western Sahara. The low-pressure system over Western Sahara likely favored the injection of dust into higher altitudes that was then transported northward to the Iberian Peninsula during 21 February. The low-pressure system dissipated on 22 February, and the high-pressure systems weakened. From 22 February and onward a predominant longitudinal baric gradient favored the transport of dust toward the east of the Iberian Peninsula and the Mediterranean Sea.

Figures S2 and S3 in the supporting information show the dust surface concentrations forecasted by NMMB/BSC-Dust model and the dust load together with the wind field at 3000 m asl forecasted by BSC-DREAM8b v2.0, respectively, during the dust outbreak. The models forecasted that dust concentrations increased from south to north as the dust plume moved northwestward on 21 February. The model forecasted that the 3000 m wind field changed on 22 February associated with the change in the synoptic situation favoring an eastward movement of the dust plume over the Iberian Peninsula toward the Mediterranean Sea and therefore increasing surface dust concentrations and dust load in the eastern regions of Spain.

3.2. Impact on Surface PM_{10} Levels

The study area has been divided into six regions, and PM_{10} hourly concentrations for each of these regions (median values) are shown in Figure 2. PM_{10} concentrations sharply increased in southern and central Spain on 21 February reaching daily concentrations $>200 \mu\text{g}/\text{m}^3$. PM_{10} levels started increasing at around 06:00 UTC in the southeastern sector, at 11:00 UTC in the southwest, and at 13:00 UTC in central Spain. At these regions, PM_{10} concentrations remained high until the 23–24 February. This spatial evolution is clearly related with the dust plume transport over the Iberian Peninsula that formed a curve-shaped plume due to the cyclonic shear imposed by the low-pressure system. Satellite images displayed in Figure S1 showed that the dust

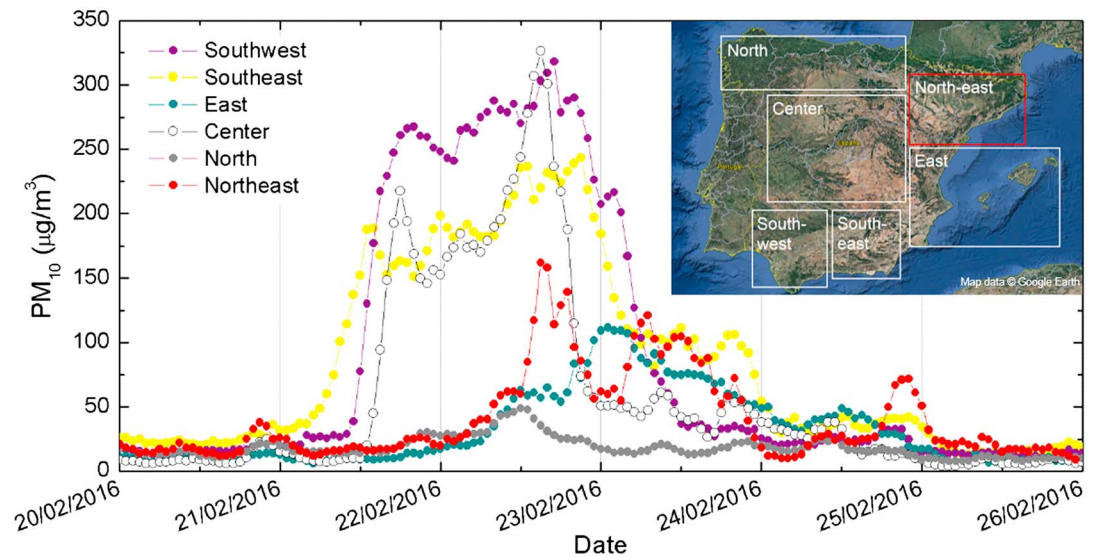


Figure 2. Hourly PM_{10} concentrations (median values) corresponding with the different regions (inset map).

plume was transported toward southern Spain in the late afternoon of 20 February. However, PM_{10} levels started increasing in the early morning of 21 February. Thus, this temporal difference might be associated with the downward movement of the aloft dust layer until it reached the surface. In general, PM_{10} concentrations were relatively low during the whole event in the north of Spain, showing a slight increase on 22 February at noon. In the northeastern sector, PM_{10} concentrations were not as high as in south and central Spain. In this region, PM_{10} showed two maxima: the first one in the afternoon of 22 February (between 15:00 and 19:00 UTC) and the second one in the morning of 23 February (around 06:00–07:00 UTC). Considering the dust plumes evolution shown in Figure S1 (EUMETSAT imagery), the first peak in PM_{10} corresponded with the dust plume moving to the northeast and the second peak with the dust plume moving eastward after passing over the Iberian Peninsula. The PM_{10} temporal evolution in the east and northeast sectors evidenced the complex dust transport scenario over these regions.

The maximum daily PM_{10} concentration decreased with latitude as shown in Figure S4. Querol *et al.* [2009] and Pey *et al.* [2013] showed that in the Mediterranean, the annual average contribution of African dust to PM_{10} decreases with latitude as well. In the dust event under study, the maximum concentrations occurred in southern Spain, with 24 h PM_{10} concentrations reaching values as high as $400 \mu\text{g}/\text{m}^3$ in some of the stations. A general relationship between maximum PM_{10} and the altitude of the station (color scale in Figure S4a) was not observed for the whole study area. Analyzing each region separately, only stations located in central Spain showed a pattern of increasing maximum daily PM_{10} concentration with altitude (correlation coefficient between PM_{10} and altitude of $R^2 = 0.48$ for AQ stations in central Spain). In a high percentage of the stations the measured concentrations were above the DL from 21 to 23 February in southern and central Spain (Figure S4b). Around 90% of the stations registered concentrations above the DL on 22 February in all regions but the northern sector, where less than 10% of the stations exceeded the DL. The number of exceedances on 24 February was significantly lower and occurred mainly in the eastern part (southeast, east, and, to a lower extent, northeast regions) associated with the temporal evolution of the dust event.

The strong spatiotemporal variability observed in PM_{10} concentrations across Spain during this dust event is also evident when downscaling and focusing on a smaller area. This is of particular interest in the northeastern region since two dust plumes overpassed this area as shown before (Figures S1 and 2). Furthermore, ancillary data on aerosol optical and physical properties and aerosol vertical distributions obtained at MSA and BCN stations (northeastern sector) will be analyzed in detail in the following sections.

Figure 3 shows the PM_{10} hourly evolution at the stations located in the northeastern sector of Spain (Catalonia), which is again split into three latitudinal subsectors. PM_{10} concentrations started increasing

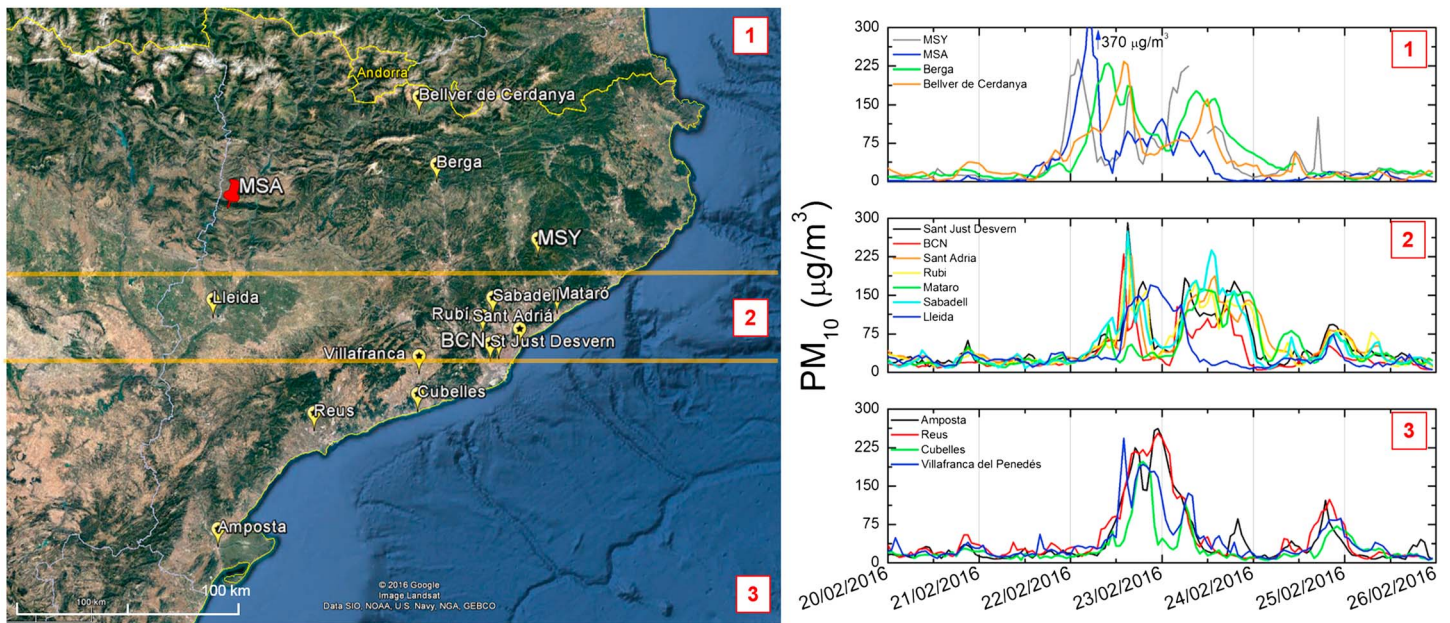


Figure 3. North-easternmost part of the Iberian Peninsula (Catalonia region) with the air quality stations marked and split into three sectors (1 = north, 2 = center, and 3 = south) and hourly PM_{10} mass concentrations at each station.

first in the northern part of Catalonia (sector 1) during the afternoon-evening of 21 February. Although in all stations included in sector 1 PM_{10} levels started increasing after mid-day, the maximum concentration occurred at different times (from first to last: MSY (Montseny), MSA, Berga, and Bellver de Cerdanya). These four stations are located at different altitudes, some of them in complex terrain, which can enhance the complexity of the dust transport and processes involved (MSY is located at 720 m asl, MSA at 1573 m asl, Berga at 649 m asl, and Bellver de Cerdanya at 1060 m asl). PM_{10} concentrations temporal evolution followed a similar pattern at all stations within sector 2 (except at Lleida) characterized by two maxima on 22 and 23 February, respectively. The magnitude of PM_{10} levels was comparable among sites in sector 2. In the southernmost part of Catalonia (sector 3), PM_{10} concentrations depicted a single (but broader) peak during the afternoon-evening of 22 February in Amposta and Reus AQ stations. At Cubelles and Villafranca AQ stations in sector 3 the PM_{10} temporal evolution was similar to that of the stations located in sector 2 but with lower concentrations during 23 February. This analysis highlights the great variability that PM_{10} levels can exhibit during Saharan dust events not only in the magnitude of the PM_{10} levels observed at each station but also in the time when PM_{10} peaks. This has been shown for the whole Spain, but such a variability is especially remarkable at a smaller scale as shown for Catalonia. This can have important repercussions when accounting for the dust contribution to PM_{10} because the selection of the background station [Escudero *et al.*, 2007] might be crucial in complex scenarios like the one presented here.

3.3. Dust Layering Structure

One of the key factors that can alter the role of dust particles in the Earth's radiation budget is their vertical distribution in the atmosphere [Sicard *et al.*, 2014]. A ceilometer located at MSA and a micropulsed lidar located at BCN allowed us to investigate the vertical structure of the aerosol layer over these two sites of northeastern Spain. Figure 4 shows the vertical and temporal evolution of the dust layer during 21 February 2016 at both sites in terms of attenuated backscatter coefficient. At the beginning of the dust event (21 February at 12:00 UTC), the aerosol vertical structure over MSA was characterized by a dust layer confined between 2000 and 3700 m asl, while simultaneously, the dust layer over BCN was located between 1200 and 3100 m asl. The temporal evolution of β_{att} at both sites was similar showing that the dust plume was progressively settling down. It can be observed that by 21 February at 14:00 UTC the MSA station was within the dust layer. Successive β_{att} profiles at MSA corresponding to 16:00 and 18:00 UTC show an increased impact of the dust plume at the MSA height (1570 m asl) and below. At BCN, due to its lower altitude close to the sea level, the dust plume took longer to reach the surface. This trend is in agreement with the temporal and spatial

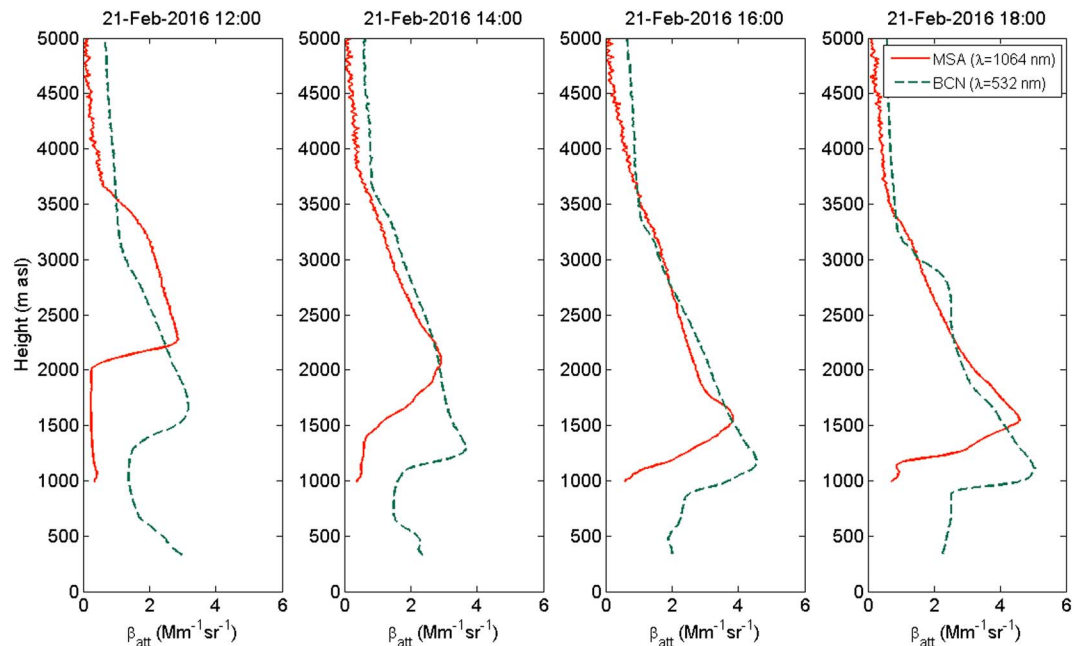


Figure 4. Vertical and temporal evolution of the attenuated backscatter coefficient, $\beta_{\text{att}}(\lambda)$, measured with ceilometer at MSA and micropulsed lidar at BCN (1 h average). Time refers to UTC.

evolution of surface PM_{10} concentration shown in Figure 3 (surface PM_{10} concentrations started increasing on 21 February at 14:00 UTC at MSA, while PM_{10} levels did not increase until the morning of 22 February at BCN). Another interesting result is the confinement at both sites of the dust plume in a low-altitude layer (< 4 km) likely coupled to the planetary boundary layer. This dust layer vertical distribution is rather low compared to vertical distributions of Saharan dust events observed in the period 2007–2012 in Barcelona [Sicard *et al.*, 2014] which show a majority of cases with dust layer heights up to 4–7 km. The good agreement obtained between the ceilometer and the MPL in the upper part of the profile is remarkable, being the lower part of the profile more influenced by topography and entrainment/mixing processes with the planetary boundary layer. Despite the wavelength difference, β_{att} profiles ($\beta_{\text{att}}(1064 \text{ nm})$ and $\beta_{\text{att}}(532 \text{ nm})$) were almost coincident in the upper part of the profiles, denoting negligible spectral dependence of the aerosol layer which is characteristic of dust particles.

3.4. Model-Measurement Comparison

Concerning the comparison of the spatiotemporal evolution forecasted by the NMMB/BSC-Dust model (Figure S2) and observed PM_{10} surface levels, the qualitative agreement was good. The model forecasted lower concentrations in the east and northeastern parts of the Iberian Peninsula, compared with south and central regions in agreement with measurements. However, from a quantitative point of view the estimated concentrations were significantly lower compared with measurements. The model forecasted PM_{10} concentrations in the range 50–200 $\mu\text{g}/\text{m}^3$ on 22 February at mid-day in southern, central, and eastern Spain. Measured concentrations were in the upper range of estimations provided by the model with significantly higher concentrations than the ones predicted by the model for the southwestern sector where PM_{10} concentrations reached values $>250 \mu\text{g}/\text{m}^3$.

The NMMB/BSC-Dust model provides forecasts of dust mass concentration vertical distribution. Normalized profiles of measured attenuated backscatter and modelled dust mass concentration have been compared for MSA and BCN (Figure 5). The aim of this comparison is to provide an estimation of the agreement between model and measurements in terms of aerosol vertical distribution. At MSA site, the agreement between model and measurements was good. At MSA, the model reproduced fairly well the shape of the dust aerosol layer on 21 February at 12:00 UTC although the center of mass calculated from the ceilometer profile was around 400 m higher than the estimated with the modelled profile. On 21 February at 18:00 UTC, the

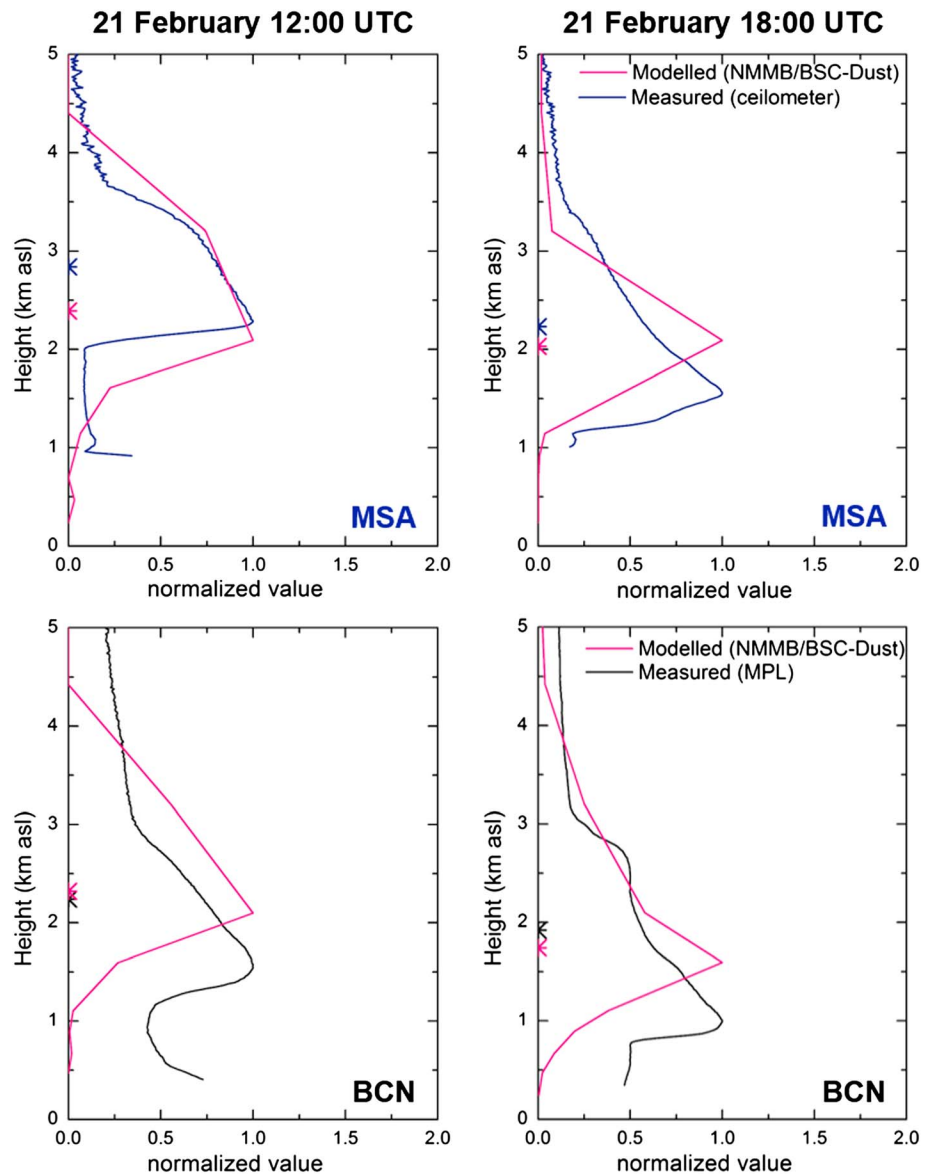


Figure 5. Vertical profiles of normalized dust concentrations forecasted by NMMB/BSC-dust model (Barcelona dust forecast center) and normalized attenuated backscattering coefficients measured over (top row) MSA and (bottom row) BCN on 21 February 2016. The asterisks correspond with the center of mass of the profile.

centers of mass estimated with both profiles differed in 200 m; however, the height of maximum dust concentration forecasted by the model was higher than measured with the ceilometer. At BCN site, the model forecasted the maximum dust concentration at higher altitudes than those observed with the MPL since the beginning of the event. The estimated centers of mass for the model and measurement profiles were in agreement with differences <100 and <200 m on 21 February at 12:00 UTC and 18:00 UTC, respectively. In general, despite the complex topography of the study area, model and measurements agreed in that the dust layer was at higher altitudes at MSA (in the pre-Pyrenees region) compared with BCN (coastal area), and the largest differences were observed in the forecasted height of maximum concentration at both sites.

4. Dust Particles Optical Properties at MSA

Figure 6 shows the attenuated backscatter coefficient, β_{att} , at 1064 nm as a function of height and time during the dust event. As mentioned in the instrumentation section, the ceilometer is 760 m downslope of

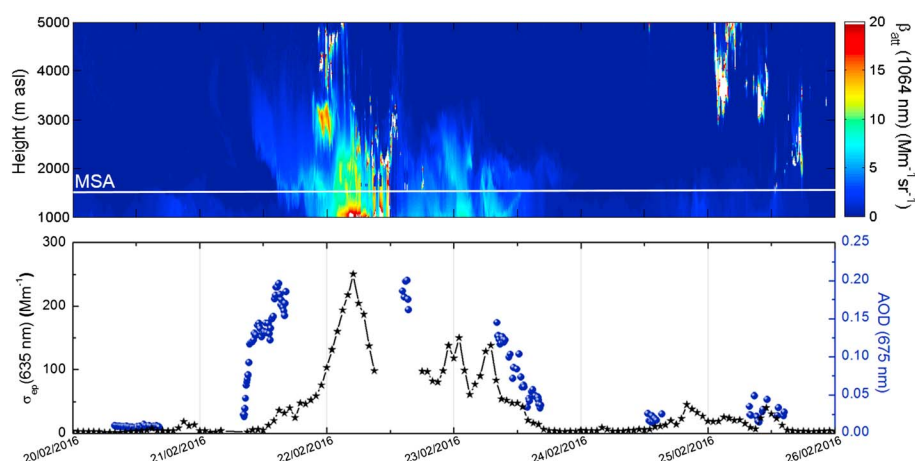


Figure 6. (top) Color map of the temporal evolution of β_{att} at 1064 nm measured with the ceilometer and the altitude of the Montsec station, MSA, marked in white and (bottom) σ_{ep} and AOD measured at MSA.

the MSA station to assure that at the height of the station the full overlap has been achieved (the altitude of the station is marked in white in Figure 6). Hourly averaged in situ aerosol light extinction coefficient, σ_{ep} , and total AOD (instantaneous data) measured at MSA station are presented in Figure 6 as well. The β_{att} evolution shows the arrival of the dust plume over the MSA station in the morning of 21 February at 2500–3500 m asl. It took around 6 h until the dust plume reached the height of the MSA station according to the ceilometer data. The β_{att} evolution agrees very well with the measurements performed at MSA station: AOD started increasing from values close to 0 up to 0.2 at around 08:00 UTC, while σ_{ep} increase did not occur until the dust plume reached the station (at around 14:00–15:00 UTC). The maximum in σ_{ep} was achieved on 22 February at 05:00 UTC. The maximum σ_{ep} (637 nm) value (hourly average of 250 Mm^{-1} at ambient conditions and 310 Mm^{-1} at standard temperature and pressure, STP) is the highest extinction coefficient measured at MSA station. At this site, the maximum hourly σ_{sp} (635 nm) and σ_{ap} (637 nm) values were 300 Mm^{-1} and 10 Mm^{-1} (at STP conditions), respectively, while for the period 2011–2013 maximum σ_{sp} (635 nm) and σ_{ap} (637 nm) were 161 Mm^{-1} and 13 Mm^{-1} , respectively [Pandolfi *et al.*, 2014b]. During African dust outbreaks, the average σ_{sp} (635 nm) and σ_{ap} (637 nm) at MSA were around 40 Mm^{-1} and 3 Mm^{-1} , respectively [Pandolfi *et al.*, 2014b]. During this event, σ_{sp} (635 nm) was $90 \pm 60 \text{ Mm}^{-1}$ during the most intense period of the event, with a maximum value of 243 Mm^{-1} at ambient conditions.

At MSA, 24 h PM_{10} samples are collected regularly every 3 days for subsequent weighing and full chemical characterization [Ripoll *et al.*, 2014]. During the analyzed period, only one filter was collected, specifically on 23 February. On this day, PM_{10} mass concentration was 97 $\mu\text{g}/\text{m}^3$, being of mineral origin 80% of the mass (77 $\mu\text{g}/\text{m}^3$ according with the chemical speciation). Knowledge of the mass scattering efficiencies of different aerosol chemical species is important since they are key parameters used to connect aerosol chemical properties and radiative properties [Seinfeld and Pandis, 1998]. To compute the mass scattering efficiency, concurrent measurements of PM_{10} mass concentration and scattering coefficient are needed. For 23 February, the mass scattering efficiency of PM_{10} particles can be calculated as the ratio of the average scattering coefficient to the PM_{10} mass concentration, obtaining a mass scattering efficiency at 525 nm of 0.5 $\text{m}^2 \text{g}^{-1}$. Assuming that only mineral matter is contributing to the scattering process, the mass scattering efficiency for mineral matter can be calculated as well, obtaining a value of 0.63 $\text{m}^2 \text{g}^{-1}$. This value is within the range of previously reported mass scattering efficiencies for mineral matter [Hand and Malm, 2007; Titos *et al.*, 2012]. With this approach, the total scattering coefficient is attributed to the mineral mass concentration, and therefore, it assumes that other species contribute marginally to the total scattering measured. This might not be completely true although mineral dust was the major constituent in PM_{10} during this day.

Despite the extremely high extinction coefficient measured at MSA during this event, AOD values were not particularly high (maximum AOD (675 nm) of 0.2). This could be attributed to the high impact of this event at low altitudes and relatively fast deposition of aloft dust layers as shown in Figure 5. As can be seen from the ceilometer data (Figures 5 and 6), the aerosol load below the MSA height was significant. Furthermore,

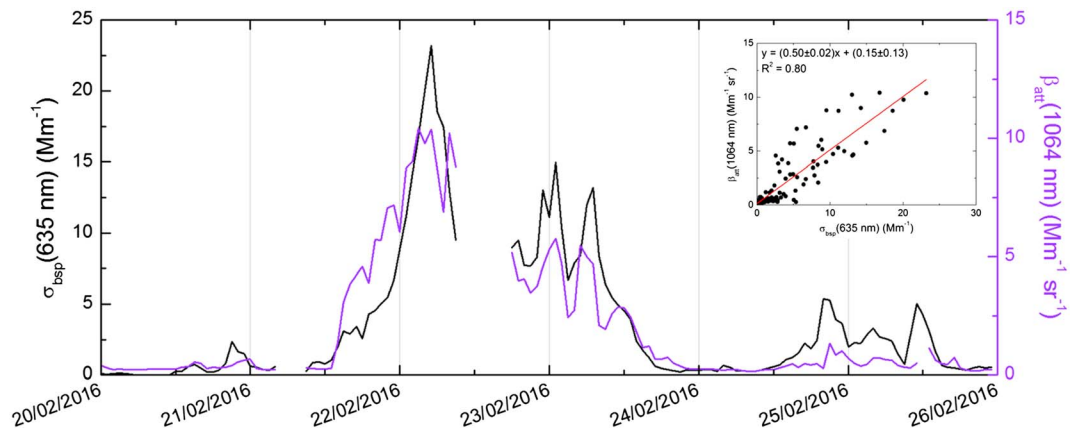


Figure 7. Time series of hourly β_{att} at 1064 nm (measured with the ceilometer) and averaged for the height level 1570 ± 15 m asl corresponding with the MSA station and σ_{bsp} at 635 nm (measured in situ with the nephelometer) at MSA station. A scatterplot of β_{att} (1064 nm) versus σ_{bsp} (635 nm) and the corresponding fitting equation is included.

it is important to take into account that by the time the maximum extinction coefficient was achieved, AOD measurements were not available, so a direct comparison of the maximum values measured in situ and with the Sun photometer is not possible. It is also probable that periods with $\text{AOD} > 0.2$ might have occurred during nighttime (21/22 and 22/23 February) when no Sun photometer data are collected or during daytime but in the presence of clouds (part of 22 February). Guerrero-Rascado *et al.* [2009] reported significantly higher AOD (675 nm) values of around 1.4, 1.2, and 0.6 at El Arenosillo, Granada, and Évora (southern Iberian Peninsula) during an extreme Saharan dust event in 2008. During moderate Saharan dust events, AOD (532 nm) of 0.28 [Bravo-Aranda *et al.*, 2015] and AOD (440 nm) of 0.6 [Obregon *et al.*, 2015] in Granada (Spain) and Évora (Portugal) have been reported, respectively. In Barcelona, Sicard *et al.* [2014] reported values of AOD (500 nm) varying between 0.17 and 0.59 for Saharan dust events observed in the period 2007–2012. When comparing AOD values among sites, it is necessary to bear in mind that AOD is a column-integrated measurement; therefore, the altitude at which the Sun photometer is located is a crucial variable that needs to be considered.

Figure 7 shows the temporal evolution of the surface hemispheric backscattering coefficient measured in situ by the nephelometer, σ_{bsp} (635 nm), and the attenuated backscattering coefficient measured with the ceilometer, β_{att} (1064 nm), at the MSA height (average β_{att} (1064 nm) at 1570 ± 15 m asl). Subplot in Figure 7 shows a scatterplot of the aforementioned variables and the respective linear fit. A good correlation between the ceilometer and nephelometer data ($R^2 = 0.80$) was obtained. Both variables followed similar temporal evolution during the dust event, detecting at the same time the beginning and end of the event as well as the main peaks. Thus, despite the intrinsic differences between variables, good agreement was achieved between the different instrumentation (active remote sensing versus in situ). The main factors that might be contributing to the uncertainty of this comparison and could introduce a bias in the comparison are as follows: (1) The use of the attenuated backscattering coefficient instead of the particle backscattering coefficient, (2) the backscattering angle at which the measurements are performed (nephelometers measure the hemispheric backscattering coefficient while the ceilometers provide the backscattering signal at 180°), (3) the different wavelengths used by each instrument (1064 nm in the ceilometer compared with 635 nm in the nephelometer); this is expected to affect the comparison differently depending on the predominant aerosol type (i.e., dust aerosols with lower spectral dependency in comparison with anthropogenic fine aerosols with higher spectral dependence), and (4) the height range of the ceilometer profile chosen for comparison with the in situ data and the horizontal distance between the ceilometer and the MSA station.

The aforementioned factors need to be further explored taking advantage of the specific experimental setup deployed at MSA in a long-term and systematic basis in order to constrain the comparison between these two instruments.

Intensive aerosol properties, both at surface level and column integrated, depicted a similar temporal trend as shown in Figure 8. Surface in situ SAE values started decreasing on 21 February but delayed with respect to

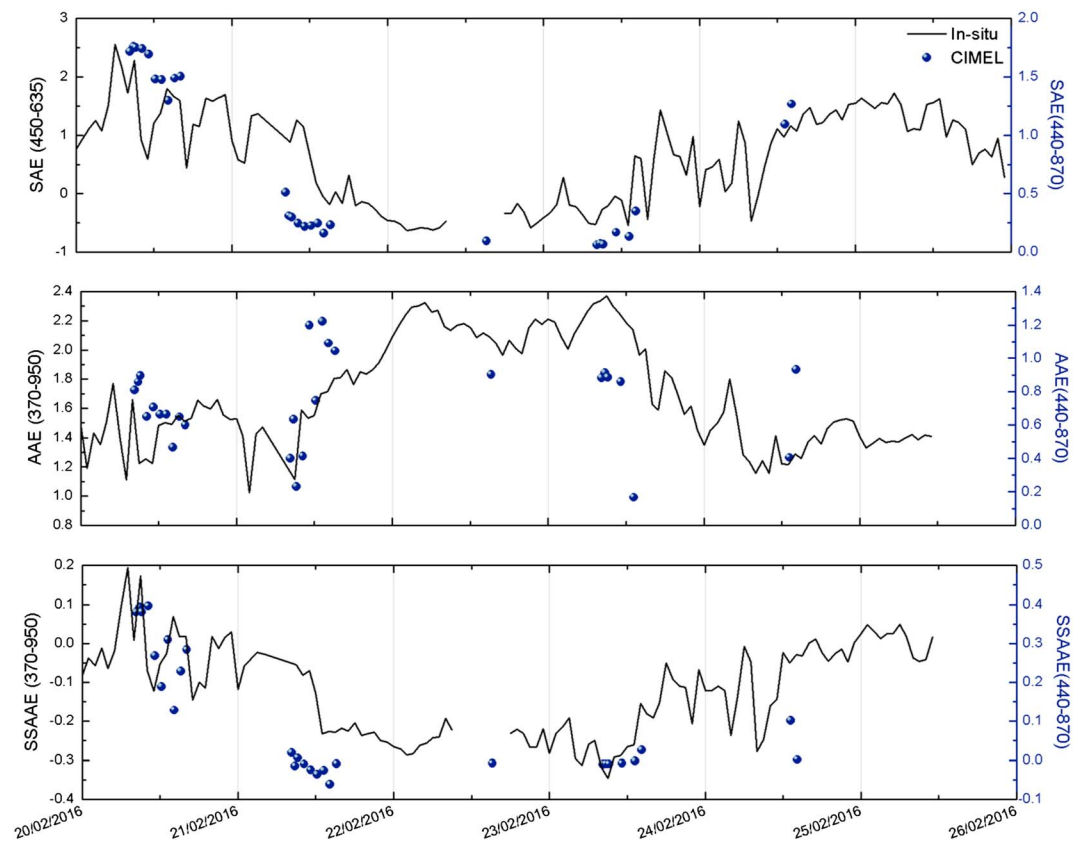


Figure 8. Temporal evolution of SAE, AAE, and SSAAE determined with in situ measurements (hourly averages) and with Sun photometer CIMEL (instantaneous data) at MSA.

the column-integrated values. This delay corresponds to the time lag since the aloft dust plume was over MSA until it reached the height of the station. Both methodologies (in situ and Sun photometer) led to values close to zero (even below zero in the case of in situ) indicating the predominance of coarse particles. The difference between in situ and columnar SAE measurements during the dust event suggests a stronger predominance of coarse particles near the ground ($SAE < 0$) than in the atmospheric column ($SAE \sim 0$). AAE values increased during the Saharan dust event reaching values up to 2.4 (surface in situ) and 1.2 (column integrated) (see Table 1). This increase in AAE denotes an absorption enhancement at shorter wavelengths that is characteristic of dust particles [e.g., *Ealo et al.*, 2016]. The difference between surface in situ and column-integrated AAE values has been reported in previous studies. For example, *Valenzuela et al.* [2015] reported in situ AAE values of 2.5 and a lower value for the entire column of 1.8 for an intense dust event in southern Spain. These differences between surface in situ and column-integrated Sun photometer AAE values can be related to the presence of particles other than dust in the atmospheric column, a frequent situation in the western Mediterranean Basin [*Pérez et al.*, 2004; *Sicard et al.*, 2016a]. Differences in the measurement technique (surface in situ versus Sun photometer) might also contribute to the observed differences in SAE and AAE.

A clear anticorrelation between in situ SAE and AAE was observed, which is characteristic of dust events indicating an increased predominance of coarser particles with enhanced absorption in the UV wavelengths. Figure S5 confirms this behavior showing that high AAE values corresponded to low PM_{10}/PM_{10} ratios not only in MSA but also in Barcelona urban area. The AAE values registered at MSA (Table 1) were significantly higher compared with the values observed previously during Saharan dust events at this site, while the SAE values were in the range of values commonly observed during previous events [*Ealo et al.*, 2016]. The SSA values measured in the visible range of the spectrum denote a predominance of scattering particles with maximum SSA of 1, both in the atmospheric column and at surface level (see Table 1). The spectral dependence of the single scattering albedo (SSAAE) decreased during the dust event as shown in Figure 8. *Ealo et al.* [2016]

Table 1. Statistical Summary Including Mean, Standard Deviation (SD) Median, Minimum and Maximum of Main Variables Measured and Derived From Column-Integrated Sun Photometer Data (Based On Instantaneous Values) and Surface In Situ Data (Based On 1 h Average) at MSA Station During the More Intense Period of the Event (21 February at 12:00 GMT to 23 February at 12:00 GMT)

Measurement Technique	Variable	Mean	SD	Median	Min	Max
Column integrated	AOD (675 nm)	0.15	0.03	0.14	0.07	0.2
	SAE (440–870 nm)	0.15	0.07	0.16	0.06	0.25
	AAE (440–870 nm)	0.95	0.14	0.90	0.74	1.2
	SSA (673 nm)	0.98	0.02	0.99	0.94	1
	SSAAE (440–870 nm)	−0.02	0.02	−0.01	−0.06	−0.008
Surface in situ	σ_{ep} (637 nm) (Mm^{-1})	94	59	83	5	250
	SAE (450–635 nm)	−0.3	0.3	−0.3	−0.6	0.7
	AAE (370–950 nm)	2.08	0.19	2.13	1.55	2.37
	SSA (637 nm)	0.95	0.01	0.96	0.90	1
	SSAAE (370–950 nm)	−0.25	0.04	−0.24	−0.35	−0.13

showed that SSAAE decreases as the contribution of dust in PM_{10} increases. SSAAE values in the range [−0.3, −0.2] as measured in situ during this dust event would correspond to an enormous presence of dust in PM_{10} of around 80 to 90% according to results from *Ealo et al.* [2016].

In general, the agreement between surface in situ and column-integrated intensive variables was good. The range of variation was larger for in situ measurements (Table 1), probably associated with higher data coverage during the most intense period of the dust event. Additionally, AERONET retrievals should be interpreted with caution due to the relatively low AOD. Despite the different intensities of the dust event over time in MSA (as shown in the extinction coefficient in Figure 6 and in PM_{10} concentrations in Figure 3), the intensive aerosol optical properties were similar as evidenced by the almost constant SAE, AAE, and SSAAE from 21 to 23 February at noon. Thus, in terms of average size and chemical composition (characterized by means of SAE, AAE, and SSAAE) the dust optical properties can be considered nearly homogeneous over time during this dust event.

4.1. Dust Size Distribution at MSA

Volume size distributions determined at MSA both in situ with the GRIMM spectrometer and in the atmospheric column with the CIMEL Sun photometer, for the period 21–23 February, are shown in Figure 9. Surface in situ data refer to 6 h averages, while Sun photometer data correspond with instantaneous data (the time is displayed in the legend in Figure 9). As depicted in Figure 9b, coarse volume concentrations increased continuously in the course of 21 February in the aloft dust layer as seen by the Sun photometer whereas at surface level they started to increase after mid-day, when the dust plume reached the MSA station. Maximum volume concentrations at surface level were achieved in the morning of 22 February, in coincidence with the maximum in the extinction coefficient (see Figure 6). Afterward, volume concentrations remained fairly constant throughout the day and decreased during 23 February, both at ground level and in the atmospheric column.

The volume size distributions measured with the GRIMM spectrometer reveal the existence of a second coarser mode for particles larger than $10 \mu m$. The main coarse mode during the event was registered at particle diameters around $3 \mu m$. Similar values have been reported for transported Saharan dust in Spain using surface in situ data [*Córdoba-Jabonero et al.*, 2011; *Sorribas et al.*, 2015], while higher diameters have been observed in aloft dust layers [*Granados-Muñoz et al.*, 2016]. Maximum volume concentrations at coarser diameters have been reported as well closer to the dust source region during the SAMUM campaign [*Toledano et al.*, 2011], at $D_p \sim 8.4 \mu m$ using surface in situ measurements. On the contrary, *Toledano et al.* [2011] showed that during SAMUM the coarse mode from Sun photometer data peaked at much lower diameters (3.4 – $4.4 \mu m$, depending on the retrieval) compared with surface in situ data. The disagreement between surface in situ and column-integrated volume size distributions during the SAMUM campaign was attributed to the vertical heterogeneity in the dust distribution [*Toledano et al.*, 2011]. In our study, agreement between the in situ and remote sensing measured volume size distributions was reasonably good once

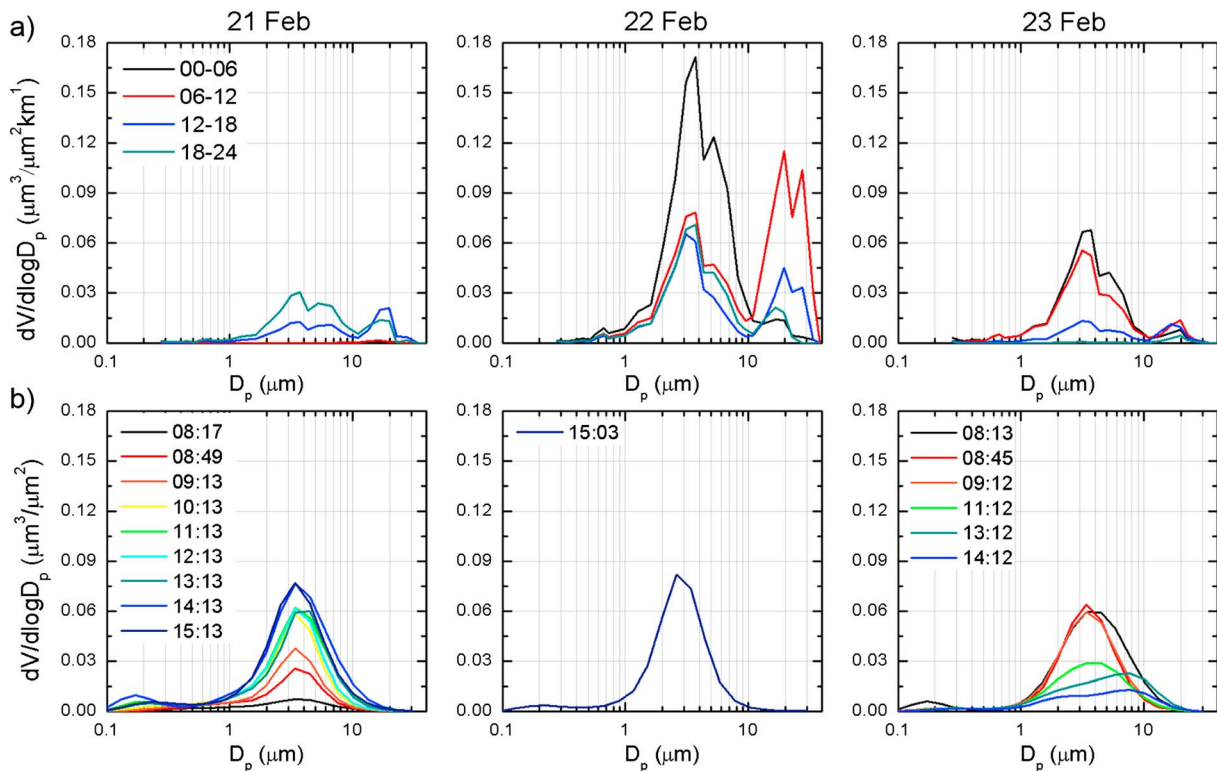


Figure 9. Volume size distributions measured (a) in situ with the GRIMM spectrometer averaged in 6 h intervals and (b) for the entire atmospheric column measured with the CIMEL Sun photometer (instantaneous data) for the period 21–23 February at MSA. Time refers to UTC.

the dust plume reached the MSA station (22 and 23 February), indicating homogeneity within the dust aerosol layer.

The shape of the volume size distribution for $D_p < 10 \mu\text{m}$ was similar, and both instruments detected the maximum concentration for particles with diameters $\sim 3 \mu\text{m}$. Surface in situ and remote sensing methodologies are not comparable when there are aloft aerosol layers as occurred on 21 February. In addition, it is necessary that the aerosol layer is homogeneous in altitude in order to achieve a good cross comparison between both techniques. Another factor that might affect the comparison between in situ and remote sensing techniques is the relative humidity (RH) since surface in situ measurements are performed at $\text{RH} < 40\%$ following WMO recommendation [World Meteorological Organization, 2003]. For the period 21–23 February the ambient RH (measured with an automatic weather station) was $50 \pm 20\%$. At these RH values, hygroscopic growth could occur which would affect the comparison between the optical spectrometer and the Sun photometer. However, dust particles are known to exhibit very low hygroscopic growth at these RHs [e.g., Fierz-Schmidhauser et al., 2010; Titos et al., 2014, 2016]. Since dust was the predominant aerosol type during the study period, the effect of hygroscopicity is expected to be negligible.

5. Conclusions

An exceptionally intense Saharan dust event affected the Iberian Peninsula during winter 2016 (20–25 February) with high impact on surface PM_{10} concentration. Overall, 90% of the AQ stations analyzed exceeded the EU PM_{10} daily limit of $50 \mu\text{g}/\text{m}^3$. Southern and central Spain were the most affected regions, with peaks as high as $400 \mu\text{g}/\text{m}^3$. The daily PM_{10} concentrations decreased with latitude. The high variability observed in PM_{10} concentrations in northeastern Spain (Catalonia) evidences the complexity of this event. In this region, the study of the spatial and vertical distribution of the dust particles shows a complex structure of the aerosol layer, being located at higher altitudes at the Pre-Pyrenees compared to the coastal area. All these features denote a strong variability in the intensity, the spatial and vertical distribution, and in the temporal evolution, which strengthen the difficulty to account for the dust contribution to PM_{10} during dust events to comply with EU Directive. Modelled vertical profiles of dust mass concentration (NMMB/BSC-Dust model)

estimated the maximum dust concentrations at higher altitude compared with measurements in MSA and BCN, while the center of mass of the dust layer was in reasonable agreement between measurements and model.

Optical and physical properties of dust particles were investigated at the continental background GAW mountain observatory of Montsec, MSA. In situ scattering Ångström exponent, SAE, values decreased to values close to zero (even below zero in the case of in situ measurements) indicating the predominance of coarse particles. Absorption Ångström exponent, AAE, values increased during the Saharan dust outbreak denoting an absorption enhancement at shorter wavelengths characteristic of dust particles. This spectral behavior of the scattering and absorption properties led to negative SSAE values throughout the event. Surface in situ SAE (AAE) values started decreasing (increasing) on 21 February but delayed with respect to the column-integrated values. This delay corresponds with the time lag since the aloft dust plume was over MSA until it reached the height of the station. In a similar manner, good agreement was found in the volume size distribution retrieved using surface in situ and passive remote sensing methodologies once the aloft dust layer reached the MSA station. The attenuated backscatter measured with the ceilometer at the MSA height (1570 ± 15 m asl) was highly correlated with the backscattering coefficient measured with the nephelometer at the MSA station. To our knowledge, this is the first time that such good agreement between surface in situ and passive and active remote sensing has been reported during a Saharan dust event. The experimental layout at Montsec with a ceilometer located downslope of the in situ station to avoid overlap issues but at a small horizontal distance is optimal to couple ceilometer with surface in situ data. Further research is needed to better understand and constrain the comparison between ceilometer and nephelometer measurements.

Acknowledgments

This work was supported by the MINECO (Spanish Ministry of Economy and Competitiveness, and FEDER funds, under the PRISMA project (CGL2012-39623-C02/00) and project TEC2015-63832-P), the MAGRAMA (Spanish Ministry of Agriculture, Food and Environment), the Generalitat de Catalunya (AGAUR 2014 SGR33, and the Departament de Territori i Sostenibilitat). This work has received funding from the European Union's Horizon 2020 Research and Innovation Programme under grant agreement 654109 (ACTRIS-2). M. Pandolfi is funded by a Ramón y Cajal Fellowship (RYC-2013-14036) awarded by the Spanish Ministry of Economy and Competitiveness. G. Titos is funded by the Spanish Ministry of Economy and Competitiveness under postdoctoral programme Juan de la Cierva-formación (FJC1-2014-20819). We thank Alberto Cazorla for in-depth discussion about the ceilometer data processing. Ana Calvo is thankfully acknowledged for helpful discussion on the optical spectrometer and providing the diameters correction. The authors acknowledge the computer resources, technical expertise, and assistance provided by the Barcelona Supercomputing Center for the BSC-DREAM8b and NMMB/BSC-Dust models. The authors express gratitude to EUMETSAT for the valuable information supplied. Thanks are due to AERONET and RIMA networks for the scientific and technical support and the Ministry of Agriculture, Food, and Environment for providing PM₁₀ data from the Spanish air quality monitoring stations. Sun photometer data have been downloaded from AERONET webpage (<http://aeronet.gsfc.nasa.gov/>). In situ data measured at MSA are accessible in a yearly basis at the World Data Center for Aerosols website (<http://ebas.nilu.no/>). All raw data used to produce the results of the paper are available from the author upon request (gloria.titos@idaea.csic.es).

References

- Anderson, T. L., et al. (1996), Performance characteristics of a high-sensitivity, three-wavelength, total scatter/backscatter nephelometer, *J. Atmos. Oceanic Technol.*, *13*, 967–986.
- Antón, M., A. Valenzuela, D. Mateos, I. Alados, I. Foyo-Moreno, F. J. Olmo, and L. Alados-Arboledas (2014), Longwave aerosol radiative effects during an extreme desert dust event in southeastern Spain, *Atmos. Res.*, *149*, 18–23.
- Basart, S., C. Perez, E. Cuevas, J. M. Baldasano, and G. P. Gobbi (2009), Aerosol characterization in northern Africa, northeastern Atlantic, Mediterranean Basin and Middle East from direct-Sun AERONET observations, *Atmos. Chem. Phys.*, *9*, 8265–8282, doi:10.5194/acp-9-8265-2009.
- Bravo-Aranda, J. A., et al. (2015), Study of mineral dust entrainment in the planetary boundary layer by lidar depolarisation technique, *Tellus B*, *67*, 26180, doi:10.3402/tellusb.v67.26180.
- Bucholtz, A. (1995), Rayleigh-scattering calculations for the terrestrial atmosphere, *Appl. Opt.*, *34*, 2765–2773.
- Burgos, M. A., D. Mateos, V. E. Cachorro, C. Toledano, and A. M. de Frutos (2016), Aerosol properties of mineral dust and its mixtures in a regional background of north-central Iberian Peninsula, *Sci. Total Environ.*, *572*, 1005–1019.
- Cabello, M., J.A.G. Orza, M.A. Barrero, E. Gordo, A. Berasaluze, L. Cantón, C. Dueñas, M.C. Fernández, and M. Pérez (2012), Spatial and temporal variation of the impact of an extreme Saharan dust event, *J. Geophys. Res.*, *117*, D11204, doi:10.1029/2012JD017513.
- Cachorro, V. E., M. A. Burgos, D. Mateos, C. Toledano, Y. Bennouna, B. Torres, A. M. de Frutos, and A. Herguedas (2016), Inventory of African desert dust events in the north-central Iberian Peninsula in 2003-2014 based on Sun-photometer-AERONET and particulate-mass-EMEP data, *Atmos. Chem. Phys.*, *16*, 8227–8248, doi:10.5194/acp-16-8227-2016.
- Campbell, J. R., D. L. Hlavka, E. J. Welton, C. J. Flynn, D. D. Turner, J. D. Spinhrine, V. S. Scott, and I. H. Hwang (2002), Full-time, eye-safe cloud and aerosol lidar observation at atmospheric radiation measurement program sites: Instruments and data processing, *J. Atmos. Oceanic Technol.*, *19*, 431–442.
- Cazorla, A., R. Bahadur, K. J. Suski, J. F. Cahill, D. Chand, B. Schmid, V. Ramanathan, and K. A. Prather (2013), Relating aerosol absorption due to soot, organic carbon, and dust to emission sources determined from in-situ chemical measurements, *Atmos. Chem. Phys.*, *13*, 9337–9350, doi:10.5194/acp-13-9337-2013.
- Chow, J. C. (1995), Measurement methods to determine compliance with ambient air quality standards for suspended particles, *J. Air Waste Manage. Assoc.*, *45*(5), 320–382, doi:10.1080/10473289.1995.10467369.
- Collaud Coen, M., E. Weingartner, D. Schaub, C. Hueglin, C. Corrigan, S. Henning, M. Schwikowski, and U. Baltensperger (2004), Saharan dust events at the Jungfraujoch: Detection by wavelength dependence of the single scattering albedo and first climatology analysis, *Atmos. Chem. Phys.*, *4*, 2465–2480, doi:10.5194/acp-4-2465-2004.
- Córdoba-Jabonero, C., et al. (2011), Synergetic monitoring of Saharan dust plumes and potential impact on surface: A case study of dust transport from Canary Islands to Iberian Peninsula, *Atmos. Chem. Phys.*, *11*, 3067–3091.
- Costabile, F., F. Barnaba, F. Angelini, and G. P. Gobbi (2013), Identification of key aerosol populations through their size and composition resolved spectral scattering and absorption, *Atmos. Chem. Phys.*, *13*, 2455–2470, doi:10.5194/acp-13-2455-2013.
- Creamean, J. M., et al. (2013), Dust and biological aerosols from the Sahara and Asia influence precipitation in the western U.S., *Science*, *339*(6127), 1572–1578, doi:10.1126/science.1227279.
- Drinovec, L., et al. (2015), The “dual-spot” Aethalometer: An improved measurement of aerosol black carbon with realtime loading compensation, *Atmos. Meas. Tech.*, *8*, 1965–1979, doi:10.5194/amt-8-1965-2015.
- Dubovik, O., and M. D. King (2000), A flexible inversion algorithm for retrieval of aerosol optical properties from sun and sky radiance measurements, *J. Geophys. Res.*, *105*, 20,673–20,696.
- Dubovik, O., A. Smirnov, B. N. Holben, M. D. King, Y. J. Kaufman, T. F. Eck, and I. Slutsker (2000), Accuracy assessment of aerosol optical properties retrieved from Aerosol Robotic Network (AERONET) Sun and sky radiance measurements, *J. Geophys. Res.*, *105*(D8), 9791–9806.

- Ealo, M., A. Alastuey, A. Ripoll, N. Pérez, M. C. Minguillón, X. Querol, and M. Pandolfi (2016), Detection of Saharan dust and biomass burning events using near-real-time intensive aerosol optical properties in the north-western Mediterranean, *Atmos. Chem. Phys.*, *16*, 12,567–12,586, doi:10.5194/acp-16-12567-2016.
- European Commission (EC) (2011), Commission staff working paper establishing guidelines for demonstration and subtraction of exceedances attributable to natural sources under the Directive 2008/50/EC on ambient air quality and cleaner air for Europe. European Commission, SEC (2011) 208 final, 37 pp. [Available at http://ec.europa.eu/environment/air/quality/legislation/pdf/sec_2011_0208.pdf.]
- Eck, T. F., B. N. Holben, J. S. Reid, O. Dubovik, A. Smirnov, N. T. O'Neill, I. Slutsker, and S. Kinne (1999), Wavelength dependence of optical depth of biomass burning, urban, and desert dust aerosols, *J. Geophys. Res.*, *104*, 31, 333–341.
- Escudero, M., S. Castillo, X. Querol, A. Avila, M. Alarcon, M. M. Viana, A. Alastuey, E. Cuevas, and S. Rodríguez (2005), Wet and dry African dust episodes over eastern Spain, *J. Geophys. Res.*, *110*, D18S08, doi:10.1029/2004JD004731.
- Escudero, M., X. Querol, J. Pey, A. Alastuey, N. Pérez, F. Ferreira, S. Alonso, S. Rodríguez, and E. Cuevas (2007), A methodology for the quantification of the net African dust load in air quality monitoring networks, *Atmos. Environ.*, *41*, 5516–5524.
- Fierz-Schmidhauser, R., P. Zieger, M. Gysel, L. Kammermann, P. F. DeCarlo, U. Baltensperger, and E. Weingartner (2010), Measured and predicted aerosol light scattering enhancement factors at the high alpine site Jungfraujoch, *Atmos. Chem. Phys.*, *10*, 2319–2333.
- Flynn, C. J., A. Mendoza, Y. Zheng, and S. Mathur (2007), Novel polarization-sensitive micropulse lidar measurement technique, *Opt. Express*, *15*, 2785–2790.
- Gkikas, A., et al. (2016), Mediterranean intense desert dust outbreaks and their vertical structure based on remote sensing data, *Atmos. Chem. Phys.*, *16*, 8609–8642.
- Granados-Muñoz, M. J., et al. (2016), A comparative study of aerosol microphysical properties retrieved from ground-based remote sensing and aircraft in situ measurements during a Saharan dust event, *Atmos. Meas. Tech.*, *9*, 1113–1133, doi:10.5194/amt-9-1113-2016.
- Grimm, H., and D. J. Eatough (2009), Aerosol measurement: The use of optical light scattering for the determination of particulate size distribution, and particulate mass, including the semi-volatile fraction, *J. Air Waste Manage. Assoc.*, *59*, 101–107, doi:10.3155/1047-3289.59.1.101.
- Guerrero-Rascado, J. L., F. J. Olmo, I. Avilés-Rodríguez, F. Navas-Guzmán, D. Pérez-Ramírez, H. Lyamani, and L. Alados Arboledas (2009), Extreme Saharan dust event over the southern Iberian Peninsula in September 2007: Active and passive remote sensing from surface and satellite, *Atmos. Chem. Phys.*, *9*, 8453–8469.
- Hand, J. L., and W. C. Malm (2007), Review of aerosol mass scattering efficiencies from ground-based measurements since 1990, *J. Geophys. Res.*, *112*, D16203, doi:10.1029/2007JD008484.
- Hansen, A. D. A., H. Rosen, and T. Novakov (1984), The aethalometer: An instrument for the real-time measurements of optical absorption by aerosol particles, *Sci. Total Environ.*, *36*, 191–196.
- Hansen, A. D. A. (2005), The aethalometer TM. Magee Scientific Company, Berkeley, California, USA. [Available at http://mageesci.com/images/stories/docs/Aethalometer_book_2005.07.03.pdf (last access: June 2016).]
- Holben, B. N., et al. (1998), AERONET—A federated instrument network and data archive for aerosol characterization, *Remote Sens. Environ.*, *66*, 1–16.
- Huneus, N., et al. (2011), Global dust model intercomparison in AeroCom phase I, *Atmos. Chem. Phys.*, *11*(15), 7781–7816, doi:10.5194/acp-11-7781-2011.
- Intergovernmental Panel on Climate Change (IPCC) (2013), Contribution of Working Group I to the Fifth Assessment Report of the Intergovernmental Panel on Climate Change, in *Summary for Policymakers in Climate Change*, edited by T. F. Stocker et al., pp. 590–600, Cambridge Univ. Press, New York.
- Kirchstetter, T. W., T. Novakov, and P. V. Hobbs (2004), Evidence that the spectral dependence of light absorption by aerosols is affected by organic carbon, *J. Geophys. Res.*, *109*, D21208, doi:10.1029/2004JD004999.
- Koren, I., Y. J. Kaufman, R. Washington, M. C. Todd, Y. Rudich, J. V. Martins, and D. Rosenfeld (2006), The Bodélé depression: A single spot in the Sahara that provides most of the mineral dust to the Amazon forest, *Environ. Res. Lett.*, *1*, 014005, doi:10.1088/1748-9326/1/1/014005.
- Lyamani, H., F. J. Olmo, and L. Alados-Arboledas (2005), Saharan dust outbreak over southeastern Spain as detected by Sun photometer, *Atmos. Environ.*, *39*, 7276–7284.
- Lyamani, H., J. Fernández-Gálvez, D. Pérez-Ramírez, A. Valenzuela, M. Antón, I. Alados, G. Titos, F. J. Olmo, and L. Alados-Arboledas (2012), Aerosol properties over two urban sites in South Spain during an extended stagnation episode in winter season, *Atmos. Environ.*, *62*, 424–432.
- Müller, T., M. Laborde, G. Kassell, and A. Wiedensohler (2011a), Design and performance of a three-wavelength LED-based total scatter and backscatter integrating nephelometer, *Atmos. Meas. Tech.*, *4*, 1291–1303, doi:10.5194/amt-4-1291-2011.
- Müller, T., et al. (2011b), Characterization and intercomparison of aerosol absorption photometers: Result of two intercomparison workshops, *Atmos. Meas. Tech.*, *4*, 245–268, doi:10.5194/amt-4-245-2011.
- Obregon, M. A., S. Pereira, V. Salgueiro, M. J. Costa, A. M. Silva, A. Serrano, and D. Bortoli (2015), Aerosol radiative effects during two desert dust events in August 2012 over the Southwestern Iberian Peninsula, *Atmos. Res.*, *153*, 404–415.
- Pandolfi, M., A. Ripoll, X. Querol, and A. Alastuey (2014b), Climatology of aerosol optical properties and black carbon mass absorption cross section at a remote high-altitude site in the western Mediterranean Basin, *Atmos. Chem. Phys.*, *14*, 6443–6460, doi:10.5194/acp-14-6443-2014.
- Pandolfi, M., A. Tobias, A. Alastuey, J. Sunyer, J. Schwartz, J. Lorente, J. Pey, and X. Querol (2014a), Effect of atmospheric mixing layer depth variations on urban air quality and daily mortality during Saharan dust outbreaks, *Sci. Total Environ.*, *494*–495, 283–289.
- Papayannis, A., D. Balis, V. Amiridis, G. Chouradakis, G. Tsaknakis, C. Zerefos, A. D. A. Castanho, S. Nickovic, S. Kazadzis, and J. Grabowski (2005), Measurements of Saharan dust aerosols over the Eastern Mediterranean using elastic-Raman lidar, spectrophotometric and satellite observations in the frame of the EARLINET project, *Atmos. Chem. Phys.*, *5*, 2065–2079.
- Papayannis, A., et al. (2007), Extraordinary dust event over Beijing, China, during April 2006: Lidar, Sun photometric, satellite observations and model validation, *J. Geophys. Res.*, *34*, L07806, doi:10.1029/2006GL029125.
- Patashnick, H., and E. G. Rupprecht (1991), Continuous PM10 measurements using the tapered element oscillating microbalance, *J. Air Waste Manage. Assoc.*, *41*(8), 1079–1083, doi:10.1080/10473289.1991.10466903.
- Pavese, G., M. Calvello, F. Esposito, L. Leone, and R. Restieri (2012), Effects of Saharan dust advection on atmospheric aerosol properties in the West-Mediterranean Area, *Adv. Meteorol.*, *2012*, 730579, doi:10.1155/2012/730579.
- Pérez, C., M. Sicard, O. Jorba, A. Comerón, and J. M. Baldasano (2004), Summertime re-circulations of air pollutants over the north-eastern Iberian coast observed from systematic EARLINET lidar measurements in Barcelona, *Atmos. Environ.*, *38*, 3983–4000.
- Perez, L., et al. (2008), Coarse particles from Saharan dust and daily mortality, *Epidemiology*, *19*(6), 800–807.
- Petzold, A., and M. Schönlinner (2004), Multi-angle absorption photometry—A new method for the measurement of aerosol light absorption and atmospheric black carbon, *J. Aerosol Sci.*, *35*, 421–441, doi:10.1016/j.jaerosci.2003.09.005.

- Pey, J., X. Querol, A. Alastuey, F. Forastiere, and M. Stafoggia (2013), African dust outbreaks over the Mediterranean Basin during 2001–2011: PM10 concentrations, phenomenology and trends, and its relation with synoptic and mesoscale meteorology, *Atmos. Chem. Phys.*, *13*, 1395–1410, doi:10.5194/acp-13-1395-2013.
- Pío, C. A., J. G. Cardoso, M. A. Cerqueira, A. Calvo, T. V. Nunes, C. A. Alves, D. Custódio, S. M. Almeida, and M. Almeida-Silva (2014), Seasonal variability of aerosol concentration and size distribution in Cape Verde using a continuous aerosol optical spectrometer, *Front. Environ. Sci.*, *2*, 15, doi:10.3389/fenvs.2014.00015.
- Prospero, J. M., P. Ginoux, O. Torres, S. E. Nicholson, and T. E. Gill (2002), Environmental characterization of global sources of atmospheric soil dust identified with the Nimbus 7 Total ozone mapping spectrometer (TOMS) absorbing aerosol product, *Rev. Geophys.*, *40*(1), 2–1–2–31, doi:10.1029/2000RG000095.
- Querol, X., A. Alastuey, J. A. Puigercus, E. Mantilla, J. V. Miro, A. Lopez-Soler, F. Plana, and B. Artiñano (1998), Seasonal evolution of suspended particles around a large coal-fired power station: Particulate levels and sources, *Atmos. Environ.*, *32*, 1963–1978.
- Querol, X., et al. (2009), African dust contributions to mean ambient PM10 mass-levels across the Mediterranean Basin, *Atmos. Environ.*, *43*, 4266–4277.
- Ripoll, A., J. Pey, M. C. Minguillón, N. Pérez, M. Pandolfi, X. Querol, and A. Alastuey (2014), Three years of aerosol mass, black carbon and particle number concentrations at Montsec (southern Pyrenees, 1570 m a.s.l.), *Atmos. Chem. Phys.*, *14*, 4279–4295, doi:10.5194/acp-14-4279-2014.
- Rodríguez, S., X. Querol, A. Alastuey, G. Kallos, and O. Kakaliagou (2001), Saharan dust contributions to PM10 and TSP levels in southern and eastern Spain, *Atmos. Environ.*, *35*, 2433–2447.
- Rodríguez, S., et al. (2011), Transport of desert dust mixed with north African industrial pollutants in the subtropical Saharan air layer, *Atmos. Chem. Phys.*, *11*, 6663–6685, doi:10.5194/acp-11-6663-2011.
- Russell, P. B., R. W. Bergstrom, Y. Shinozuka, A. D. Clarke, P. F. DeCarlo, J. L. Jimenez, J. M. Livingston, J. Redemann, O. Dubovik, and A. Strawa (2010), Absorption Angstrom exponent in AERONET and related data as an indicator of aerosol composition, *Atmos. Chem. Phys.*, *10*, 1155–1169.
- Salvador, P., B. Artiñano, F. Molero, M. Viana, J. Pey, A. Alastuey, and X. Querol (2013), African dust contribution to ambient aerosol levels across central Spain: Characterization of long-range transport episodes of desert dust, *Atmos. Res.*, *127*, 117–129.
- Salvador, P., S. Alonso-Pérez, J. Pey, B. Artiñano, J. J. de Bustos, A. Alastuey, and X. Querol (2014), African dust outbreaks over the western Mediterranean Basin: 11-year characterization of atmospheric circulation patterns and dust source areas, *Atmos. Chem. Phys.*, *14*, 6759–6775, doi:10.5194/acp-14-6759-2014.
- Schuster, G. L., O. Dubovik, and B. N. Holben (2006), Angstrom exponent and bimodal aerosol size distributions, *J. Geophys. Res.*, *111*, D07207, doi:10.1029/2005JD006328.
- Seinfeld, J. H., and S. N. Pandis (1998), *Atmospheric Chemistry and Physics: From Air Pollution to Climate Change*, pp. 1100–1200, John Wiley, Hoboken, N. J.
- Sicard, M., S. Bertolin, M. Mallet, P. Dubuisson, and A. Comerón (2014), Estimation of mineral dust longwave radiative forcing: Sensitivity study to particle properties and application to real cases in the region of Barcelona, *Atmos. Chem. Phys.*, *14*, 9213–9231, doi:10.5194/acp-14-9213-2014.
- Sicard, M., R. Barragan, F. Dulac, L. Alados-Arboledas, and M. Mallet (2016a), Aerosol optical, microphysical and radiative properties at regional background insular sites in the western Mediterranean, *Atmos. Chem. Phys.*, *16*, 12,177–12,203, doi:10.5194/acp-16-12177-2016.
- Sicard, M., R. Izquierdo, M. Alarcón, J. Belmonte, A. Comerón, and J. M. Baldasano (2016b), Near-surface and columnar measurements with a micro pulse lidar of atmospheric pollen in Barcelona, Spain, *Atmos. Chem. Phys.*, *16*, 6805–6821, doi:10.5194/acp-16-6805-2016.
- Sorribas, M., J. A. Ogren, F. J. Olmo, A. Quirantes, R. Fraile, M. Gil-Ojeda, and L. Alados-Arboledas (2015), Assessment of African desert dust episodes over the southwest Spain at sea level using in situ aerosol optical and microphysical properties, *Tellus B*, *67*, 27482, doi:10.3402/tellusb.v67.27482.
- Spinhirne, J. D. (1993), Micro pulse lidar, *IEEE Trans. Geosci. Remote Sens.*, *31*, 48–55.
- Tegen, I., A. A. Lacis, and I. Fung (1996), The influence on climate forcing of mineral aerosol from disturbed soils, *Nature*, *380*, 419–422.
- Titos, G., I. Foyo-Moreno, H. Lyamani, X. Querol, A. Alastuey, and L. Alados-Arboledas (2012), Optical properties and chemical composition of aerosol particles at an urban location: An estimation of the aerosol mass scattering and absorption efficiencies, *J. Geophys. Res.*, *117*, D04206, doi:10.1029/2011JD016671.
- Titos, G., H. Lyamani, A. Cazorla, M. Sorribas, I. Foyo-Moreno, A. Wiedensohler, and L. Alados-Arboledas (2014), Study of the relative humidity dependence of aerosol light-scattering in southern Spain, *Tellus B*, *66*, 24536, doi:10.3402/tellusb.v66.24536.
- Titos, G., A. Cazorla, P. Zieger, E. Andrews, H. Lyamani, M. J. Granados-Muñoz, F. J. Olmo, and L. Alados-Arboledas (2016), Effect of hygroscopic growth on the aerosol light-scattering coefficient: A review of measurements, techniques and error sources, *Atmos. Environ.*, *141*, 494–507.
- Toledano, C., V. E. Cachorro, A. M. de Frutos, M. Sorribas, and N. Prats (2007), Inventory of African Desert dust events over the southwestern Iberian Peninsula in 2000–2005 with an AERONET Cimel Sun photometer, *J. Geophys. Res.*, *112*, D21201, doi:10.1029/2006JD008307.
- Toledano, C., et al. (2011), Optical properties of aerosol mixtures derived from sun-sky radiometry during SAMUM-2, *Tellus B*, *63B*, 635–648, doi:10.1111/j.1600-0889.2011.00573.x.
- Valenzuela, A., F. J. Olmo, H. Lyamani, M. Antón, A. Quirantes, and L. Alados-Arboledas (2012a), Analysis of the desert dust radiative properties over Granada using principal plane sky radiances and spheroids retrieval procedure, *Atmos. Res.*, *104–105*, 292–301.
- Valenzuela, A., F. J. Olmo, H. Lyamani, M. Antón, A. Quirantes, and L. Alados-Arboledas (2012b), Classification of aerosol radiative properties during African desert dust intrusions over southeastern Spain by sector origins and cluster analysis, *J. Geophys. Res.*, *117*, D06214, doi:10.1029/2011JD016885.
- Valenzuela, A., F. J. Olmo, H. Lyamani, M. Antón, G. Titos, A. Cazorla, and L. Alados-Arboledas (2015), Aerosol scattering and absorption Angstrom exponents as indicators of dust and dust-free days over Granada (Spain), *Atmos. Res.*, *154*, 1–13.
- Wiegner, M., F. Madonna, I. Biniotoglou, R. Forkel, J. Gasteiger, A. Geiss, G. Pappalardo, K. Schafer, and W. Thomas (2014), What is the benefit of ceilometers for aerosol remote sensing? An answer from EARLINET, *Atmos. Meas. Tech.*, *7*, 1979–1997.
- World Meteorological Organization (2003), Aerosol measurement procedures guidelines and recommendations, *GAW Rep. 153*, 72 pp., Geneva, Switzerland.